ANGLE-OF-ATTACK IMPACT ON THE AEROTHERMODYNAMIC PERFORMANCE OF FLAT-NOSE POWER-LAW BODIES IN HYPERSONIC AIRFLOW

Wilson F. N. Santos
Combustion and Propulsion Laboratory
National Institute for Space Research
Cachoeira Paulista, SP 12630–000 BRAZIL

Keywords: *DSMC, Hypersonic Flow, Rarefied Flow, Power-Law Shape, Angle of Attack*

Abstract

This work describes a computational investigation on rarefied hypersonic flow past flat-nose power-law leading edges at incidence. Positive angle-of-attack effects on the aerodynamic surface quantities have been investigated by employing the Direct Simulation Monte Carlo (DSMC) Method. A method that properly accounts for the non-equilibrium aspects of the flow that arise near the leading-edge nose and that are especially important at high Mach numbers. The study is of great importance since it is impossible to achieve ideally sharp leading edges of airframes such as waverider vehicles. The results presented highlight the sensitivity of heat flux, drag and lift to changes not only on the angle of attack but also on the afterbody surface of the leading edges defined by power-law shapes. The analysis showed that positive angle of attack causes the expected asymmetry in the flow patterns as the stagnation point moves from the symmetry axis to the windward side of the leading edges.

1 Introduction

An increasingly important problem in aerospace engineering is that of predicting aerodynamic characteristics of vehicles flying at very high speeds and high altitudes. The problems related to the aerothermodynamics at high flight Mach numbers have recently received the attention of several investigations because of their importance in connection with hypersonic vehicles and re-entry problems. Hypersonic vehicles are generally characterized by slender bodies and sharp leading edges in order to achieve good aerodynamic properties like high lift and low drag. Nevertheless, at high Mach numbers, the vehicle leading edges should be sufficiently blunt in order to reduce the heat transfer rate to acceptable levels, and possibly to allow for internal heat conduction. In addition, as aerodynamic heating may cause serious problems at these speeds, the removal of heat near the front of the leading edge must be considered, since the stagnation region is one of the most thermally stressed zones. Therefore, designing a hypersonic vehicle leading edge involves a tradeoff between making the leading edge sharp enough to obtain acceptable aerodynamic and propulsion efficiency and blunt enough to reduce the aerodynamic heating in the stagnation point.

Recently, considerable attention has been given to the problem of calculating aerodynamic characteristics of power-law bodies $(y \propto x^n, 0 < n < 1)$ at hypersonic speed [1-9]. The major interest in these works has gone into considering the power-law shape as possible candidates for blunting geometries of hypersonic leading edges, such as hypersonic waverider vehicles [10], which have been lately considered for high-altitude/low-density applications [11-

14]. The interest in power-law shape is based on the work of Mason and Lee [15], who have pointed out that, for certain exponents, power-law shapes exhibit aerodynamic properties similar to geometrically sharp shapes. They suggested the possibility of a difference between shapes that are geometrically sharp and shapes that behave aerodynamically as if they were sharp.

Of particular significance on power-law shapes are the works by Santos and Lewis [2-8]. Through the use of DSMC method, they found that the stagnation point heating behavior for power law leading edges with finite radius of curvature ($n = 1/2$) followed that predicted for classical blunt body in that the heating rate on blunt bodies is inversely proportional to the square root of curvature radius at the stagnation point. For those power-law leading edges with zero radii of curvature ($n > 1/2$), it was found that the stagnation point heating is not a function of the curvature radius in the vicinity of the leading edges, but agreed with the classical blunt body behavior predicted by the continuum flow far from the stagnation point. Results were compared to a corresponding circular cylinder to determine which geometry would be better suited as a blunting profile. Their analysis also showed that power-law shapes provided smaller total drag and smaller shock wave standoff distance than the circular cylinder, typically used in blunting sharp leading edges for heat transfer considerations. However, circular cylinder still provided smaller stagnation point heating than the power-law shapes under the range of conditions investigated.

In order to improve the stagnation point heating of power-law shapes, a modification was introduced into the power-law leading edge. The new leading edge consisted of a flat nose followed by an afterbody surface given by a power-law shape, and defined as the flat-nose power-law leading edge. This concept is based on the work of Reller [16], who showed that a method of designing low heat transfer bodies is devised on the premise that the rate of heat transfer to the nose will be low if the local velocity is low, while the rate of heat transfer to the afterbody will be low if the local density is low. A typical body that results from this design method consists of a flat nose followed by a highly curved, but for the most part slightly inclined, afterbody surface.

In this context, Santos [17-20] has examined the aerodynamic surface quantities for a family of these new contours, flat-nose power-law leading edges. The emphasis of the works was to compare the performance of these new contours with that for power-law leading edges with zero-thickness nose (Santos and Lewis [2]). The thickness effect was examined for a range of Knudsen number, Kn_t, based on the leading edge thickness, covering from the transitional flow regime to the free molecular flow one. It was examined a group of shapes that combined Kn_t of 1, 10 and 100 and power-law exponents of 2/3, 3/4 and 4/5. The analysis showed that flat-nose power-law leading edges provided much smaller stagnation point heating and slightly larger total drag than the zero-thickness power-law shapes under the range of conditions investigated.

These works[17-20] on hypersonic flow past flat-nose power-law shapes have been concentrated primarily on the analysis of the flowfield structure, shock-wave structure and aerodynamic surface quantities by considering the idealized situation of two-dimensional rarefied hypersonic flow at zero angle of incidence. Nevertheless, for positive angle of attack, important changes occur in the flowfield structure and in the aerodynamic surface quantities on blunt leading edges. This involves the modification of the flowfield properties and shock strength and, consequently, some effects on aerodynamic forces acting on, and on heat transfer to the body surface. Moreover, the knowledge of these properties at zero angle of attack is not sufficient to predict with certainty the flow characteristics over these shapes with incidence.

In this connection, the primary purpose of this work is to investigate the impact of the angle of attack on the behavior of the aerodynamic surface quantities. The essential characteristics of the angle of attack effect on the stagnation point heating, total drag and lift on the flat-nose

power-law bodies will be examined for positive angle of attack with 5, 10, 15 and 20 degrees of incidence. In an intermediate or transition rarefied gas regime, the complete investigation of the flowfield structure would require the full formulation of kinetic theory. The governing equation in the transition regime is the Boltzmann equation. Nevertheless, in order to circumvent the difficult of a direct solution of the Boltzmann equation, in the current study, the DSMC method will be employed to calculate the rarefied hypersonic two-dimensional flow.

2 Leading Edge Geometry Definition

In dimensional form, the power-law contours that define the shapes of the afterbody surfaces are given by the following expression,

$$y = y_{nose} + ax^n \qquad (1)$$

where y_{nose} is the half thickness of the flat nose of the leading edges, n is the power-law exponent and a is the power-law constant which is a function of n.

The flat-nose power-law shapes are modeled by assuming a sharp leading edge (wedge) of half angle θ with a circular cylinder of radius R inscribed tangent to this wedge. The flat-nose power-law shapes, inscribed between the wedge and the cylinder, are also tangent to both shapes at the same common point where they have the same slope angle. It was assumed a leading edge half angle of 10 degrees, a circular cylinder diameter of 10^{-2}m, power-law exponents of 2/3, 3/4, and 4/5, and front surface thicknesses t/λ_∞ of 0.01, 0.1 and 1, where $t = 2y_{nose}$ and λ_∞ is the freestream molecular mean free path. Figure 1 shows schematically this construction.

From geometric considerations, the power-law constant a is obtained by matching slopes for the wedge, circular cylinder and flat-nose power-law body at the tangency point. The common body height H at the tangency point is equal to $2R\cos\theta$, and the body length L from the nose to the tangency point in the axis of symmetry is given by $n(H-t)/2\tan\theta$. Since the wake region behind the leading edges is not of interest in this

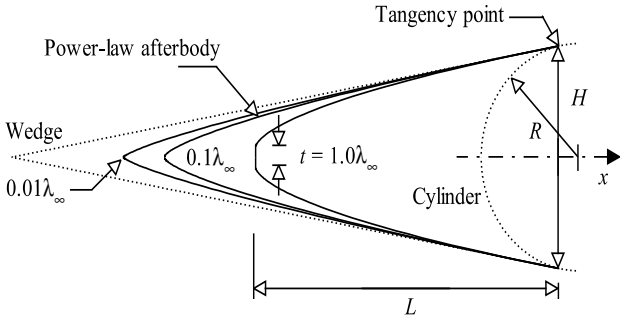

Fig. 1 Drawing illustrating the leading-edge shapes.

investigation, it was assumed that the flat-nose power-law bodies are infinitely long but only the length L is considered.

3 Computational Method and Procedure

The Direct Simulation Monte Carlo (DSMC) method, pioneered by Bird [21], has become one of the standard and reliable successful numerical techniques for modeling complex flows in the transition flow regime. The transition regime is the category of flow that falls between the continuum regime, where the Navier-Stokes equations are valid, and the free molecular regime, which is the limit of infinite Knudsen number.

In the DSMC method, a group of representative molecules are tracked as they move, collide and undergo boundary interactions in simulated physical space. Each simulated molecule represents a very much larger number of real molecules. The molecular motion, which is considered to be deterministic, and the intermolecular collisions, which are considered to be stochastic, are uncoupled over the small time step used to advance the simulation and computed sequentially. The time step should be chosen to be sufficiently small in comparison with the local mean collision time [21]. In general, the total simulation time, divided into time steps, is identified with the physical time of the real flow.

In the present account, molecular collisions are modeled by the variable hard sphere (VHS) molecular model [22] and by the no time counter (NTC) collision sampling technique [23]. The

mechanics of the energy exchange processes between kinetic and internal modes for rotation and vibration are controlled by the Borgnakke-Larsen statistical model [24]. The essential feature of this model is that part of collisions is treated as completely inelastic, and the remainder of the molecular collisions is regarded as elastic. Simulations are performed using a non-reacting gas model consisting of two chemical species, N_2 and O_2. The vibrational temperature is controlled by the distribution of energy between the translational and rotational modes after an inelastic collision. The rates of rotational and vibrational relaxation are dictated by collision numbers Z_R and Z_V, respectively. The collision numbers are traditionally given as constants, 5 for rotation and 50 for vibration.

In order to implement the particle-particle collisions, the flowfield is divided into an arbitrary number of regions, which are subdivided into computational cells. The cells are further subdivided into four subcells, two subcells/cell in each direction. The cell provides a convenient reference sampling of the macroscopic gas properties, whereas the collision partners are selected from the same subcell for the establishment of the collision rate.

The computational domain used for the calculation is made large enough so that body disturbances do not reach the upstream and side boundaries, where freestream conditions are specified. A schematic view of the computational domain is depicted in Fig. 2. Side I is defined by the body surface. Diffuse reflection with complete surface thermal accommodation is the condition applied to this side. Side II is the freestream side through which simulated molecules enter and exit. Finally, the flow at the downstream outflow boundary, side III, is predominantly supersonic and vacuum condition is specified [21]. At this boundary, simulated molecules can only exit.

Numerical accuracy in DSMC method depends on the grid resolution chosen as well as the number of particles per computational cell. The effect of grid resolution on computed results is of particular interest for the present study because insufficient grid resolution can reduce significantly the accuracy of the predicted aerodynamic heating and forces acting on the body surface. Hence, heat transfer, pressure and skin friction coefficients are used as the representative parameters for the grid sensitivity. Grid independence was tested by running the calculations with half and double the number of cells in ξ and η directions (see Fig. 2) compared to a standard grid. Solutions (not shown) were near identical for all grids used and were considered fully grid independent.

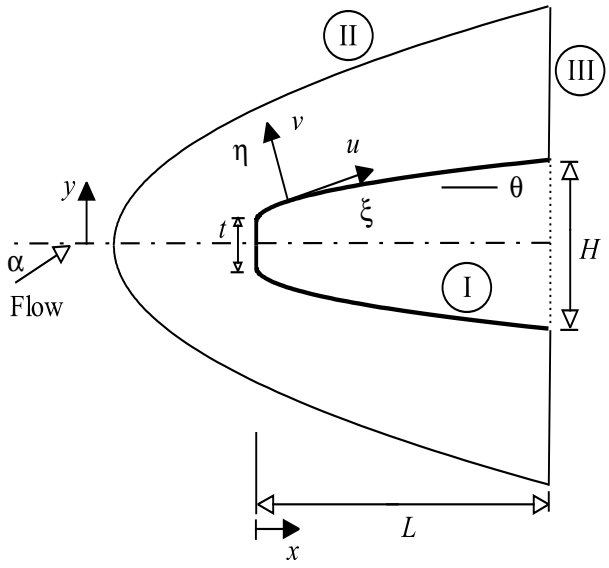

Fig. 2 Schematic view of the computational domain.

4 Freestream and Flow Conditions

The flow conditions represent those experienced by a spacecraft at an altitude of 70 km. This altitude is associated with the transitional regime, which is characterized by the overall Knudsen number of the order of or larger than 10^{-2}.

The freestream flow conditions used for the numerical simulation of flow past the leading edges are those given by Santos [17] and summarized in Table 1, and the gas properties [21] are tabulated in Table 2.

Referring to Table 2, m, d, X, and ω stand, respectively, for the mass fraction, molecular mass,

molecular diameter and the viscosity index.

The freestream velocity V_∞ is assumed to be constant at 3.5 km/s, which correspond to a freestream Mach number M_∞ of 12. The leading-edge surface has a constant wall temperature T_w of 880 K for all cases considered. This wall temperature represents the temperature usually attained in an actively-cooled metallic leading edge. Furthermore, these flow conditions may represent the top end of an ascending hypersonic trajectory as well as be representative of a maneuvering reentry vehicle.

The overall Knudsen number Kn_t, defined as λ_∞/t, corresponds to 100, 10 and 1 for leading-edge thickness, t/λ_∞ of 0.01, 0.1 and 1, respectively. It is important to mention that $t/\lambda_\infty = 0$ case ($Kn_t = \infty$) corresponds to the power-law leading edge already investigated by Santos and Lewis [2]. Finally, the Reynolds number Re_t covers the range from 0.193 to 19.3, based on conditions in the undisturbed stream with leading-edge thickness t as the characteristic length.

In order to simulate the angle-of-attack effect, the DSMC calculations were performed independently for four distinct numerical values of α, i.e., 5, 10, 15 and 20 degrees. Again, it is important to mention that $\alpha = 0$ represents the case investigated previously by Santos [17].

Table 1 Freestream and flow conditions

Parameter	Value	Unit
Temperature (T_∞)	220.0	K
Pressure (p_∞)	5.582	N/m^2
Density (ρ_∞)	8.753×10^{-5}	kg/m^3
Viscosity (μ_∞)	1.455×10^{-5}	Ns/m^2
Number density (n_∞)	1.8209×10^{21}	m^{-3}
Mean free path (λ_∞)	9.03×10^{-4}	m

Table 2 Gas properties

Parameter	O_2	N_2	Unit
m	5.312×10^{-26}	4.65×10^{-26}	kg
d	4.010×10^{-10}	4.11×10^{-10}	m
X	0.237	0.763	
ω	0.77	0.74	

5 Computational Results and Discussion

Aerodynamic surface quantities of particular interest are number flux, heat transfer, pressure, skin friction, drag and lift. Therefore, the purpose of this section is to discuss and to compare differences in the profiles of these properties, expressed in coefficient form, due to changes on the angle of attack.

The number flux N is calculated by sampling the molecules impinging on the surface by unit time and unit area. The dependence of the number flux on the angle of attack α is shown in Figs. 3(a,b) for leading edge defined by $Kn_t = 1$ and $n = 2/3$. In this set of plots, Fig. 3(a) represents the number flux along the windward side of the leading edge, and Fig. 3(b) that in the leeward side. Also, the number flux N is normalized by $n_\infty V_\infty$, and S is the arc length s, normalized by the freestream mean free path λ_∞, measured from the stagnation point along the body surface for the case corresponding to angle of attack of 0 degree.

According to these plots, it is observed that by increasing the incidence causes the expected asymmetry in the flow patterns as the stagnation point moves from the symmetry axis to the windward side of the body surface. The dimensionless number flux decreases along the frontal and afterbody surfaces on the leeward side with increasing the incidence. In contrast, along the windward side, the number flux decreases on the frontal surface and increases on the afterbody surface with the angle of attack rise.

The heat flux q_w to the body surface is calculated by the net energy flux of the molecules impinging on the surface. The net heat flux q_w is related to the sum of the translational, rotational and vibrational energies of both incident and reflected molecules. A flux is regarded as positive if it is directed toward the body surface. The heat flux is normalized by $\rho_\infty V_\infty^3/2$ and presented in

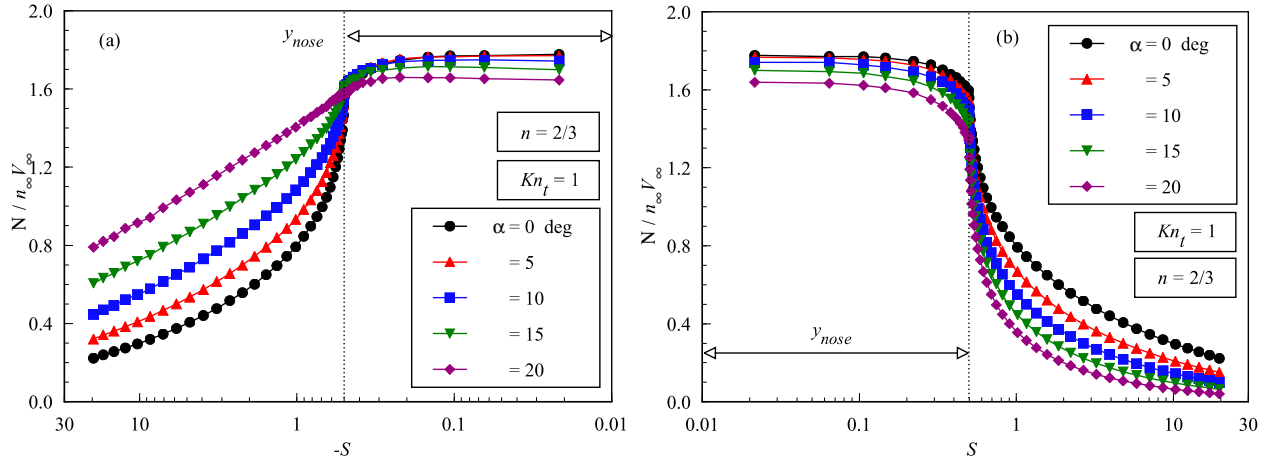

Fig. 3 Effect of the angle of attack on number flux $N/n_\infty V_\infty$ along the (a) windward side and (b) leeward side of body surface.

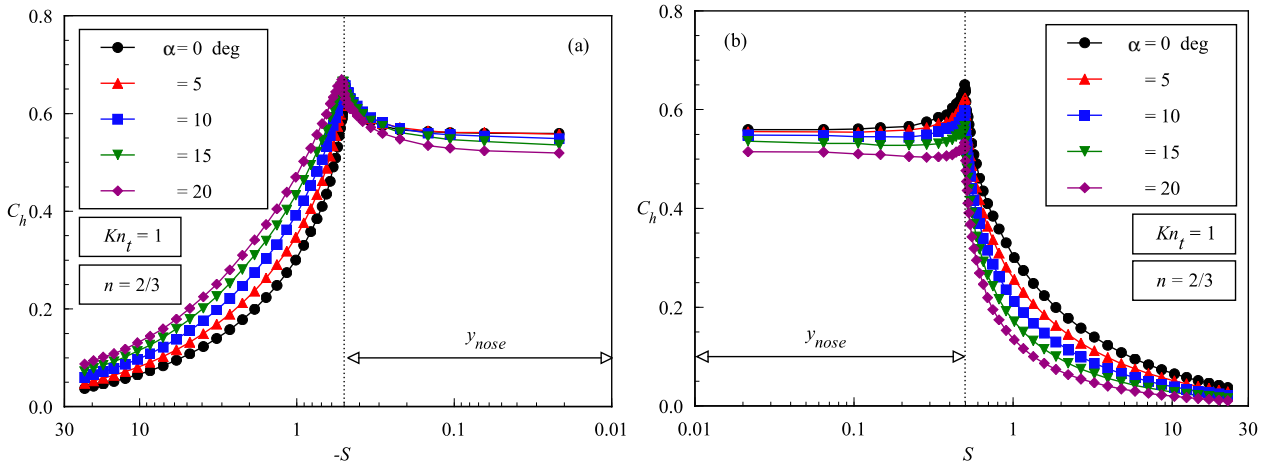

Fig. 4 Effect of the angle of attack on heat transfer coefficient C_h along the (a) windward side and (b) leeward side of body surface.

terms of heat transfer coefficient C_h.

The effect of changing the angle of attack α on the heat transfer coefficient C_h along the windward and leeward sides is plotted in Figs. 4(a,b), respectively, as a function of the dimensionless arc length S. According to these plots, the heat transfer coefficient remains essentially constant over the first half of the front surface, but then increases at the vicinity of the flat-face/afterbody junction for this flattest case investigated, $Kn_t = 1$ ($t/\lambda_\infty = 1$). Subsequently, the heat transfer coefficient decreases sharply and continues to decline along the body surface. Similar to the number flux, the net heat transfer coefficient decreases with increasing α along the leeward surface for the cases shown, as would be expected due to the flow expansion. Nevertheless, on the windward side, the heat transfer coefficient decreases along the frontal surface and presents the expected behavior along the afterbody surface in that it increases with increasing the incidence. Again, an expected behavior due to the flow compression on this side of the leading edges.

Usually, the stagnation region is generally considered as being the most thermally stressed zone in sharp/blunt bodies, as shown by the

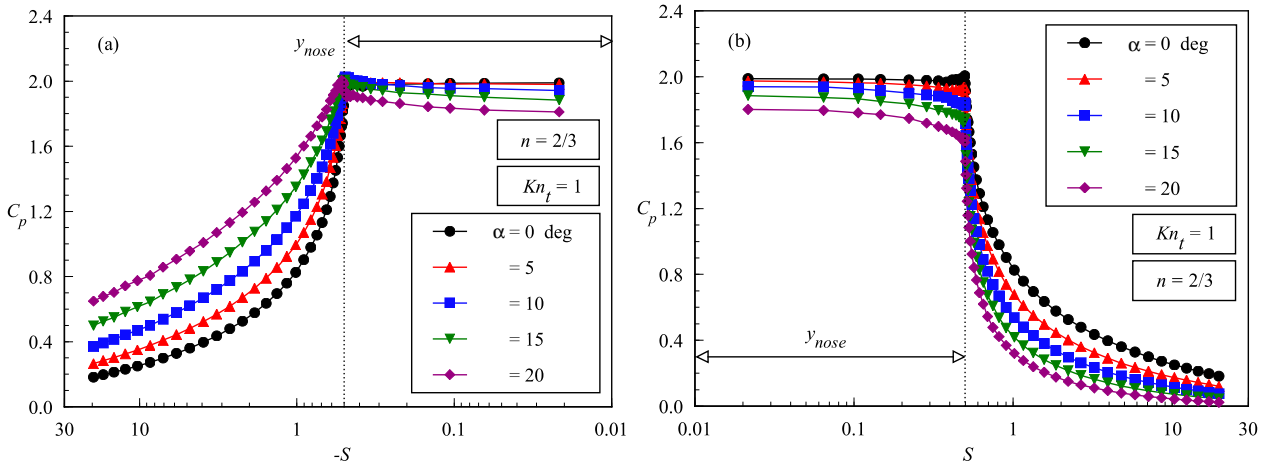

Fig. 5 Effect of the angle of attack on pressure coeffi cient C_p along the (a) windward side and (b) leeward side of body surface.

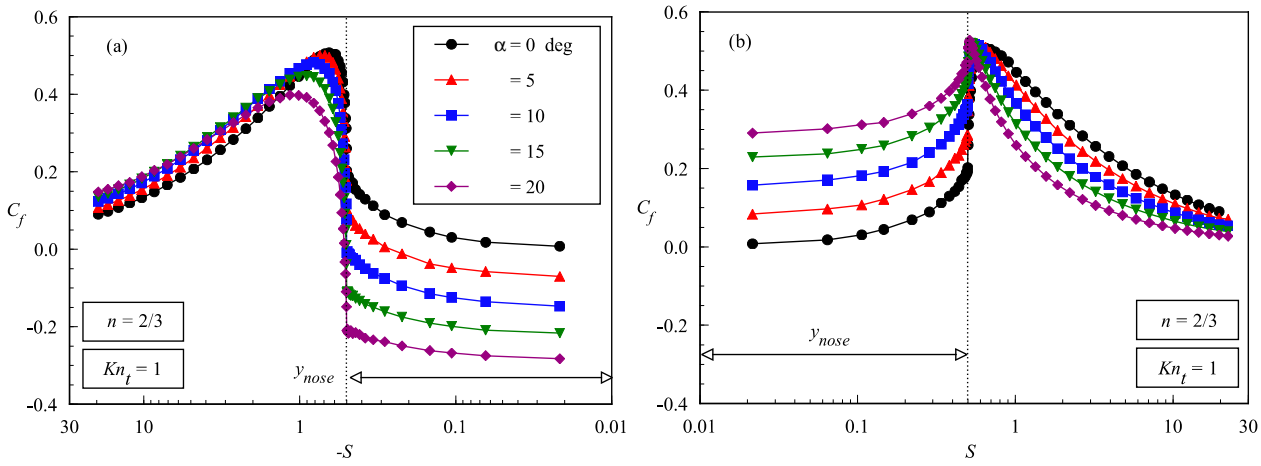

Fig. 6 Effect of the angle of attack on skin friction coeffi cient C_f along the (a) windward side and (b) leeward side of body surface.

power-law cases, defi ned by $Kn_t = \infty$ ($t/\lambda_\infty = 0$), investigated by Santos and Lewis [2]. Nonetheless, as a flat nose is introduced into these power law shapes, the most severe heat transfer region moves to the flat-face/afterbody junction as shown in Figs. 4(a,b).

The pressure p_w on the body surface is calculated by the sum of the normal momentum fluxes of both incident and reflected molecules at each time step. Results are presented in terms of the pressure coeffi cient C_p defi ned as being $2(p_w - p_\infty)/\rho_\infty V_\infty^2$.

The variation of the pressure coeffi cient C_p caused by changes on the angle of attack α is illustrated in Figs. 5(a,b). In this set of diagrams, Fig. 5(a) stands for the pressure coeffi cient along the windward side of the leading edge, and Fig. 5(b) for that on the leeward side. It can be noted from these fi gures that the pressure coeffi cient is high along the front surface, basically a constant value along it, and decreases dramatically along the afterbory surface. Furthermore, at the vicinity of the flat-face/afterbody junction, the pressure coeffi cient decreases on the leeward side and slightly increases on the windward side with increasing the incidence.

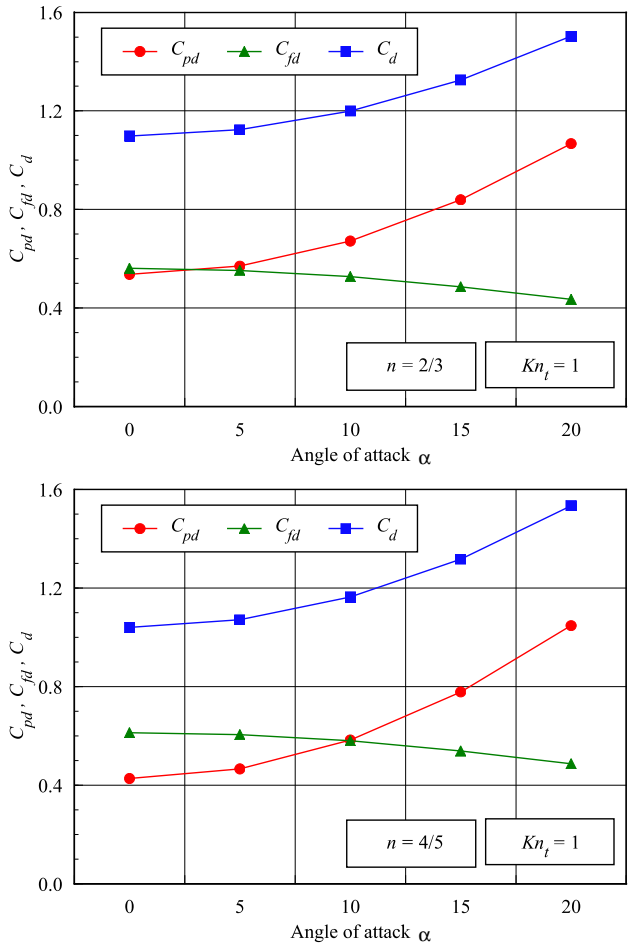

Fig. 7 Pressure drag C_{pd}, skin friction drag C_{fd} and total drag coeffi cient C_d as a function of the angle of attack for Kn_t of 1 and afterbody shape n of (a) 2/3 and (b) 4/5.

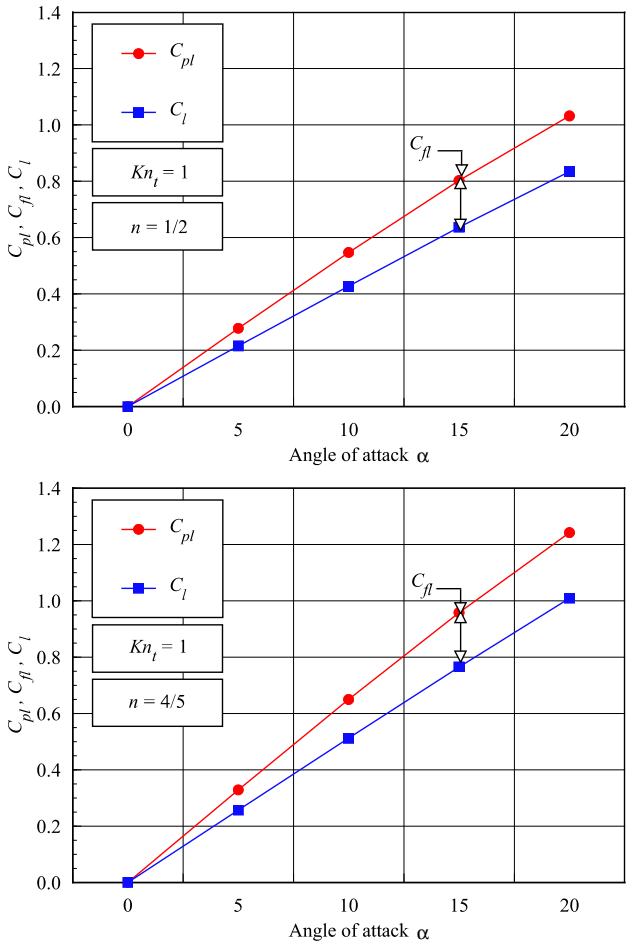

Fig. 8 Pressure lift C_{pl}, skin friction lift C_{fl} and total lift coeffi cient C_l as a function of the angle of attack for Kn_t of 1 and afterbody shape n of (a) 2/3 and (b) 4/5.

The shear stress τ_w on the body surface is calculated by averaging the tangential momentum transfer of the molecules impinging on the surface. The shear stress τ_w on the body surface is normalized by $\rho_\infty V_\infty^2/2$ and presented in terms of the dimensionless skin friction coeffi cient C_f.

It is important to mention that for the diffuse reflection model imposed for the gas-surface interaction, reflected molecules have a tangential moment equal to zero, since the molecules essentially lose, on average, their tangential velocity component.

The dependence of the skin friction coeffi cient C_f attributed to variations on the angle of attack α is depicted in Figs. 6(a,b) for the case combined by flat-face thickness of Kn_t = 1 and afterbody shape of n = 2/3. According to these plots, for zero angle of incidence, the skin friction coeffi cient C_f is zero at the stagnation point and increases along the front surface up to the flat-face/afterbody junction of the leading edge. After that, C_f increases meaningfully to a maximum value that depends on the angle of attack, and decreases downstream along the afterbody surface.

At incidence, a different behavior is noticed for the skin friction coeffi cient not only on the frontal surface but also on the afterbody surface. It is immediately evident from Figs. 6(a,b) that changes in the angle of attack α from 10 to 20 degree produce substantial differences in the mag-

nitude of the skin friction coefficient, particularly in a region of the body surface that corresponds to a body slope angle around of 45 degrees (peak value). The direction of change is toward larger skin friction coefficient at the vicinity of the flat-face/afterbody junction on the leeward side and toward lower skin friction coefficient around the same station on the windward side. It may be recognized from these plots that the skin friction coefficient C_f is negative along the windward side of the frontal face for angle of attack $\alpha > 0$. It means that the force due to the shear stress is in the opposite direction as compared to that acting on the afterbody surface along the windward side.

The drag on a surface in a gas flow results from the interchange of momentum between the surface and the molecules colliding with the surface. The total drag is obtained by the integration of the pressure p_w and shear stress τ_w distributions from the stagnation point of the leading edge to the station L that corresponds to the tangent point common to all the leading edges (see Fig. 1). It is important to mention that the values for the total drag were obtained by assuming the shapes acting as leading edges. Therefore, no base pressure effects were taken into account on the calculations. Results for total drag are normalized by $\rho_\infty V_\infty^2 H/2$ and presented as total drag coefficient C_d and its components of pressure drag coefficient C_{pd} and the skin friction drag coefficient C_{fd}.

The impact of the changes on the total drag coefficient C_d with increasing the angle of attack α is illustrated in Figs. 7(a,b). In this set of diagrams, Fig. 7(a) presents the drag coefficient for the case represented by $Kn_t = 1$ and afterbody shape $n = 2/3$, and Fig. 7(b) for that of $Kn_t = 1$ and afterbody shape $n = 4/5$. It is seen that as the angle of attack increases the contribution of the pressure drag C_{pd} to the total drag increases and the contribution of the skin friction drag C_{fd} decreases. The reason for that is because the leading edges becomes blunt as seen from the freestream with increasing the incidence.

For comparison purpose, the results for total drag coefficient for flat-nose power-law leading edges corresponding to thickness Knudsen number $Kn_t = 1$ and afterbody shapes given by power-law exponent n of 2/3, 3/4 and 4/5 are tabulated in Table 3 as a function of the angle of attack α. According to Table 3, it is observed that the total drag coefficient slightly decreases with increasing the power-law exponent n. In addition, as would be expected, the total drag significantly increases with the angle-of-attack rise.

Table 3 Total drag coefficient C_d as a function of the angle of attack α for leading-edge thickness corresponding to Kn_t of 1.

α	$n = 2/3$	$n = 3/4$	$n = 4/5$
0	1.098	1.059	1.040
5	1.123	1.088	1.071
10	1.200	1.174	1.164
15	1.326	1.317	1.317
20	1.503	1.519	1.534

Table 4 Total lift coefficient C_l as a function of the angle of attack α for leading-edge thickness corresponding to Kn_t of 1.

α	$n = 2/3$	$n = 3/4$	$n = 4/5$
5	0.216	0.243	0.257
10	0.428	0.483	0.511
15	0.637	0.721	0.765
20	0.835	0.949	1.009

Similar to total drag, results for total lift is normalized by $\rho_\infty V_\infty^2 H/2$ and presented as lift coefficient C_l and its components of pressure lift coefficient C_{pl} and skin friction lift coefficient C_{fl}.

The sensitivity of the lift coefficient C_l with incidence is demonstrated in Figs. 8(a,b). In this set of figures, Fig. 8(a) presents the lift coefficient for the case represented by $Kn_t = 1$ and afterbody shape $n = 2/3$, and Fig. 8(b) for that of $Kn_t = 1$ and afterbody shape $n = 4/5$. According to this set of figures, the lift coefficient shows an expressive rise with increasing the angle of attack α dictated by the pressure contribution.

In what follows, it proves convenient to tab-

ulate the results for total lift coefficient for flat-nose power-law leading edges. In this way, the lift coefficient for leading edges corresponding to thickness Knudsen number $Kn_t = 1$ and afterbody shapes given by power-law exponent n of 2/3, 3/4 and 4/5 are tabulated in Table 4 as a function of the angle of attack α. Referring to Table 4, it is observed that the total lift coefficient slightly increases with increasing the power-law exponent n. In contrast, the total lift significantly increases with the angle-of-attack rise, as expected.

6 Concluding Remarks

Computations of a rarefied hypersonic flow on blunt bodies have been performed by using the Direct Simulation Monte Carlo method. The calculations provided information concerning the nature of the aerodynamic surface quantities for a family of contours composed by a flat nose followed by a curved afterbody surface defined by power-law shapes. Effects of the angle of attack on the number flux, heat transfer, pressure coefficient, skin friction coefficient, drag coefficient, and lift coefficient were investigated for a range of 0 to 20 degrees. The thickness of the frontal surface considered in this study covered hypersonic flow from the transitional flow regime to the free molecular flow regime.

Calculations showed that the stagnation point moved from the symmetry axis to the flat-face/afterbody junction on the windward side of the body surface at incidence. In addition, it was found that the total drag slightly decreased as the power-law afterbody shape changed from 2/3 to 4/5. Also, the analysis showed that the total lift coefficient increased with increasing the angle of attack.

The calculations presented in this work have only covered a limited number of parametric variations. Further calculations with additional combinations of leading-edge thickness and afterbody shape might provide more insight into the sensitivity of the aerodynamic surface quantities to the angle of attack. This is of great importance since blunt leading edges at incidence will allow leakage of the high-pressure lower surface flow into the upper surface region, causing a reduction in the lift coefficient as compared to sharp leading edges, a major concern in the design and prediction of flowfields over hypersonic waveriders.

7 Acknowledgments

The financial support provided by FAPESP (Fundação de Amparo à Pesquisa do Estado de São Paulo), grant No. 2003/01765-9, is gratefully acknowledged.

References

[1] O'Brien, T. F. and Lewis, M. J., "Power law shapes for leading-edge blunting with minimal shock standoff." *Journal of Spacecraft and Rockets*, Vol. 36, No. 5, pp. 653–658, 1999.

[2] Santos, W. F. N., and Lewis, M. J., "Angle of attack effect on rarefied hypersonic flow over power law shaped leading edges." in *23rd International Symposium on Rarefied Gas Dynamics*, Whistler, BC, Canada, July 20-25, 2002.

[3] Santos, W. F. N., and Lewis, M. J., "Power law shaped leading edges in rarefied hypersonic flow." *Journal of Spacecraft and Rockets*, Vol. 39, No. 6, pp. 917–925, 2002.

[4] Santos, W. F. N., and Lewis, M. J., "Aerodynamic heating performance of power law leading edges in rarefied hypersonic flow." in *36th AIAA Thermophysics Conference*, AIAA Paper 2003–3894, Orlando, FL, June 23-26, 2003.

[5] Santos, W. F. N., and Lewis, M. J., "Effects of compressibility on rarefied hypersonic flow over power law leading edges." in *42nd AIAA Aerospace Sciences Meeting and Exhibit*, AIAA Paper 2004–1181, Reno, NV, January 5-8, 2004.

[6] Santos, W. F. N., and Lewis, M. J., "DSMC calculations of rarefied hypersonic flow over power law leading edges with incomplete surface accommodation." in *34th AIAA Fluid Dynamics Conference and Exhibit*, AIAA Paper 2004–2636, Portland, OR, June 28–July 1, 2004.

[7] Santos, W. F. N., and Lewis, M. J., "Calculation of shock wave structure over power law bodies in hypersonic flow." *Journal of Spacecraft and Rockets*, Vol. 42, No. 2, pp. 213–222, 2005 (Also as AIAA Paper 2003–1134 in *41st AIAA*

Aerospace Sciences Meeting and Exhibit, Reno, NV, 2003.)

[8] Santos, W. F. N., and Lewis, M. J., "Aerothermodynamic performance analysis of hypersonic flow on power law leading edges." *Journal of Spacecraft and Rockets*, Vol. 42, No. 4, pp. 588–597, 2005.

[9] Boyd, I. D., and Padilla, J. F., "Simulation of sharp leading edge aerothermodynamic." in *12th AIAA International Space Planes and Hypersonic Systems and Technologies*, AIAA Paper 2003–7062, Norfolk, VA, 15–19 December, 2003.

[10] Nonweiler, T. R. F., "Aerodynamic problems of manned space vehicles." *Journal of the Royal Aeronautical Society*, Vol. 63, Sept, pp. 521–528, 1959.

[11] Anderson, J. L., "Tethered aerothermodynamic research for hypersonic waveriders." in *Proceedings of the 1st International Hypersonic Waverider Symposium*, Univ. of Maryland, College Park, MD, 1990.

[12] Potter, J. L. and Rockaway, J. K., "Aerodynamic optimization for hypersonic flight at very high altitudes." in *Rarefied gas Dynamics: Space Science and Engineering*, edited by B. D. Shizgal and D. P. Weaver, Vol. 160, Progress in Astronautics and Aeronautics, AIAA New York, pp.296-307, 1994.

[13] Rault, D. F. G., "Aerodynamic characteristics of a hypersonic viscous optimized waverider at high altitude." *Journal of Spacecraft and Rockets*, Vol. 31, No. 5, pp. 719–727, 1994.

[14] Graves, R. E. and Argrow, B. M., "Aerodynamic performance of an osculating-cones waverider at high altitudes." in *35th AIAA Thermophysics Conference*, AIAA Paper 2001-2960, Anaheim, CA, 2001.

[15] Mason, W. H. and Lee, J., "Aerodynamically blunt and sharp bodies." *Journal of Spacecraft and Rockets*, Vol. 31, No. 3, pp. 378–382, 1994.

[16] Reller Jr., J. O., "Heat transfer to blunt nose shapes with laminar boundary layers at high supersonic speeds." NACA RM-A57FO3a, 1957.

[17] Santos, W. F. N., "Aerothermodynamic characteristics of flat-nose power-law bodies in low-density hypersonic flow." in *22nd AIAA Applied Aerodynamics Conference and Exhibit*, AIAA Paper 2004–5381, Providence, RI, 16–19 August, 2004.

[18] Santos, W. F. N., "Structure of shock wave on flat-nose power-law bodies." in *43rd AIAA Aerospace Sciences Meeting and Exhibit*, AIAA Paper 2005–0968, Reno, NV, January 10-13, 2005.

[19] Santos, W. F. N., "Some extensions to the aerothermodynamic performance study of flat-nose power-law bodies." in *43rd AIAA Aerospace Sciences Meeting and Exhibit*, AIAA Paper 2005–0969, Reno, NV, January 10-13, 2005.

[20] Santos, W. F. N., "Influence of gas-surface interaction on hypersonic aerothermodynamic performance of flat-nose power-law bodies." in *44th AIAA Aerospace Sciences Meeting and Exhibit*, AIAA Paper 2006–1194, Reno, NV, January 9-12, 2006.

[21] Bird, G. A., *Molecular Gas Dynamics and the Direct Simulation of Gas Flows*, Oxford University Press, Oxford, England, UK, 1994.

[22] Bird, G. A., "Monte Carlo simulation in an engineering context." in *Progress in Astronautics and Aeronautics: Rarefied gas Dynamics*, edited by Sam S. Fisher, Vol. 74, part I, AIAA New York, pp. 239–255, 1981.

[23] Bird, G. A., "Perception of numerical method in rarefied gasdynamics." in *Rarefied gas Dynamics: Theoretical and Computational Techniques*, edited by E. P. Muntz, and D. P. Weaver and D. H. Capbell, Vol. 118, Progress in Astronautics and Aeronautics, AIAA, New York, pp. 374–395, 1989.

[24] Borgnakke, C. and Larsen, P. S., "Statistical collision model for Monte Carlo simulation of polyatomic gas mixture." *Journal of Computational Physics*, Vol. 18, No. 4, pp. 405–420, 1975.